

Mol Pharm. Author manuscript; available in PMC 2014 January 07.

Published in final edited form as:

Mol Pharm. 2013 January 7; 10(1): 33-42. doi:10.1021/mp300240m.

Increased tumor homing and tissue penetration of the filamentous plant viral nanoparticle Potato virus X

Sourabh Shukla^{1,#}, Amber L. Ablack^{4,#}, Amy M. Wen¹, Karin L. Lee¹, John D. Lewis⁴, and Nicole F. Steinmetz^{1,2,3,*}

¹Department of Biomedical Engineering, Case Western Reserve University, 10900 Euclid Ave., Cleveland, OH 44106, USA

²Department of Radiology, Case Western Reserve University, 10900 Euclid Ave., Cleveland, OH 44106, USA

³Department of Materials Science and Engineering, Case Western Reserve University, 10900 Euclid Ave., Cleveland, OH 44106, USA

⁴Translational Prostate Cancer Research Group, University of Alberta, 5-142C Katz Group Building, 114th St and 87th Ave, Edmonton, AB T6G 2E1 CANADA

Abstract

Nanomaterials with elongated architectures have been shown to possess differential tumor homing properties compared to their spherical counterparts. Here, we investigate whether this phenomenon is mirrored by plant viral nanoparticles that are filamentous (Potato virus X) or spherical (Cowpea mosaic virus). Our studies demonstrate that Potato virus X (PVX) and Cowpea mosaic virus (CPMV) show distinct biodistribution profiles and differ in their tumor homing and penetration efficiency. Analogous to what is seen with inorganic nanomaterials, PVX shows enhanced tumor homing and tissue penetration. Human tumor xenografts exhibit higher uptake of PEGylated filamentous PVX compared to CPMV, particularly in the core of the tumor. This is supported by immunohistochemical analysis of the tumor sections, which indicates greater penetration and accumulation of PVX within the tumor tissues. The enhanced tumor homing and retention properties of PVX along with its higher payload carrying capacity makes it a potentially superior platform for applications in cancer drug delivery and imaging applications.

Keywords

viral nanoparticles; nanoparticle shape; tumor homing; tissue penetration; potato virus X; cowpea mosaic virus; tumor xenografts

^{*}Corresponding author: Prof. Nicole F. Steinmetz, Ph.D., Mt. Sinai Scholar, Department of Biomedical Engineering, Radiology, Materials Science and Engineering, Case Western Reserve University School of Medicine, 10900 Euclid Avenue, Cleveland, OH 44106, USA, phone: 216-368-5590, nicole.steinmetz@case.edu. #both authors contributed equally to the work

INTRODUCTION

Recent data indicate advantages of filamentous nanomaterials for *in vivo* medical applications

The ability of nanoparticles to carry large drug payloads and the ease with which ligands can be added so that the payload is delivered to specific target sites (i.e. cancer or cardiovascular disease) make them particularly promising for biomedical applications. The chemical composition and physical properties of nanomaterials such as shape and elasticity can significantly impact their fates in vivo. Recent studies indicate that filamentous nanomaterials have superior pharmacokinetic and tumor-homing properties 1–7. Still, the vast majority of platform technologies currently under development consist of spherical or elongated low aspect ratio materials (AR < 5). While carbon-based nanotubes and filomicelles are notable exceptions, carbon nanotubes have low biocompatibility ⁸ and filomicelles are in the micron-size regime ⁵. Physically and chemically tailoring materials at the nanoscale in two dimensions to create high aspect ratio materials is challenging using synthetic materials, mainly due to polydispersity and poorly controlled chemistry. Efforts in synthetic chemistry and nanotechnology have sought to mimic characteristics such as selfassembly and programmability at the atomic level that nature has already achieved. Therefore, we have adopted a bio-inspired approach to engineer viral nanoparticles (VNPs) from plants for imaging and drug delivery.

Plant viral nanoparticles and nanofilaments as platforms for diagnostics and therapeutics

VNP technology has previously been exploited to develop gene therapy vectors, vaccines, and oncolytic virotherapies ^{9–11}. Plant VNPs are considered safe from a human health perspective because they are not pathogenic in mammals ^{12, 13}. VNPs come in many shapes and sizes and each species is truly monodisperse, highly symmetrical and the structure is known to atomic precision. VNPs can be engineered with targeting ligands, drugs and/or imaging molecules ¹⁴. Several VNPs are currently being developed for nanomedical applications, where the vast majority of platforms under investigation are of spherical nature, e.g. the *Human papilloma virus* (HPV)-based Gardasil vaccine, *Adenovirus*-based gene-delivery vectors, and various plant viruses including *Cowpea mosaic virus* (CPMV), *Brome mosaic virus* (BMV), *Cowpea chlorotic mottle virus* (CCMV), *Hibiscus chlorotic ringspot virus* (HCSRV), and *Red clover necrotic mottle virus* (RCNMV) ^{12, 15–24}. In contrast, few high aspect ratio VNPs have been investigated. Those that have, including *Tobacco mosaic virus* and bacteriophage M13, have focused mainly on *in vitro* tissue engineering applications ^{25–27}.

In this work we explore the high aspect ratio, filamentous plant VNP *Potato virus X* (PVX) and compare its biodistribution and tumor homing properties to the 30 nm-sized icosahedral *Cowpea mosaic virus* (CPMV). CPMV has been extensively studied and developed, and its *in vivo* properties are well understood $^{13, 28-30}$. It can be regarded as a prototype VNP for *in vivo* medical applications. *Potato virus X* (PVX) is an emerging filamentous VNP platform being developed for nanomedical applications in our laboratory. These VNP platforms can be engineered and tailored for desired applications through genetic modification or bioconjugate chemistry. CPMV nanoparticles consist of 60 copies of each a small and large protein and offer 300 reactive Lys side chains per particle 31 , which can be functionalized using *N*-hydroxysuccinimidyl ester (NHS)-activated probes and linkers. PVX nanofilaments measure 515×13 nm (AR 40), and consist of 1270 identical coat protein units. We have previously shown that essentially all 1270 coat proteins can be chemically addressed via their reactive Lys side chains using NHS chemistry 32 .

A side-by-side evaluation of CPMV nanoparticles and PVX nanofilaments in preclinical animal tumor models is reported here. Specifically, the tumor homing efficiency and biodistribution of these VNP formulations are evaluated in human fibrosarcoma, squamous carcinoma, and colon cancer xenograft tumors in both chicken chorioallantoic membrane (CAM) and mouse models.

EXPERIMENTAL SECTION

CPMV and **PVX** propagation

CPMV was propagated in cowpea plants (Vigna unguiculata). Plants were infected with 100 ng/µl CPMV in 0.1 M potassium phosphate buffer (pH 7.0) by mechanical inoculation using a light dusting of carborundum; leaves were harvested 10-14 days post infection and purified using established procedures ³³. Virus concentration in plant extracts was determined by UV/visible spectroscopy (ϵ_{CPMV} =8.1 mLmg⁻¹cm⁻¹). PVX was propagated in Nicotiana benthamiana, leaves were harvested 10-14 days post infection. Purification was as follows: 100 g of leaves were homogenized in a standard blender using 2 volumes of cold 0.5 M borate buffer (pH 7.8) and filtered through 2-3 layers of cheesecloth and pH was adjusted to 6.5 using 1 M HCl. 0.2% (w/v) ascorbic acid and 0.2% (w/v) sodium sulfite were added. Plant material was centrifuged at 5,500 g for 20 min and supernatant was collected. After adding NaCl 0.2 M and 8% (w/v) PEG (MW 8,000), the solution was centrifuged at 15,000 g for 15 min and the pellet was resuspended in 0.1% β-mercaptoethanol and 0.5 M urea followed by centrifugation at 8,000 g for 30 min. The supernatant was ultracentrifuged at 160,000 g for 3 hrs, then the pellet was resuspended in 5 mL buffer overnight at 4°C and ultracentrifuged over a 10-40% sucrose gradient at 100,000 g for 2 hrs. The light scattering band was collected and dialyzed against 0.5 M borate buffer (pH 7.8). Virus concentration in plant extracts was determined by UV/visible spectroscopy (ϵ_{PVX} =2.97 mLmg⁻¹cm⁻¹).

Bioconjugate chemistry to modify CPMV and PVX with A647 and PEG

CPMV and PVX (at 2 mgmL⁻¹ in 0.1 M potassium phosphate buffer pH 7.0) were reacted with NHS-PEG5000 (NanoCS) and NHS-A647 (Invitrogen) using a one-pot synthesis protocol (Figure 1A). Reagents were added in a 10% (v/v) final concentration of DMSO and incubated overnight at room temperature, with agitation. PEG and A647 (or A555) were added using a molar excess of 3,000 and 2,000, respectively, per CPMV. For PVX, a molar excess of 4,000 and 2,500 of PEG and A647 (or A555), respectively was added. CPMV has a molar mass of 5.6×10⁶ gmol⁻¹, and PVX has a molar mass of 35×10⁶ gmol⁻¹. VNP formulations were purified through dialysis and 10 kDa-cut off centrifugal filter units (Millipore). A647-CPMV-PEG5000 nanoparticles and A647-PVX-PEG5000 nanofilaments were characterized using a combination of UV/visible spectroscopy, fluorescence measurements, denaturing gel electrophoresis, zeta potential measurements, and transmission electron microscopy (TEM).

UV/visible spectroscopy

The number of A647 or A555 molecules per virion was determined by UV/visible spectroscopy measurement done using the NanoDrop. The particle concentrations were determined using VNP-specific extinction coefficients of 8.1 mLmg $^{-1}$ cm $^{-1}$ (CPMV) and 2.97 mLmg $^{-1}$ cm $^{-1}$ (PVX) at 260 nm.

Denaturing gel electrophoresis

SDS gel electrophoresis was carried out to analyze conjugation of PEG chains to individual coat proteins. 10 µg protein samples were analyzed on 4–12% NuPage gels (Life Technologies) in 1X MOPS SDS running buffer. Protein bands were visualized under white light after staining the gels with Coomassie blue (0.25% w/v).

Zeta potential measurements

Zeta potential measurements were carried out using a 90 Plus zeta potential analyzer (Brookhaven Instruments Co., USA) for A647-CPMV-PEG5000 nanoparticles and A647-PVX-PEG5000 nanofilaments (1.5 mL of a 0.1 mgmL $^{-1}$ and 0.05 mg mL $^{-1}$ solutions, respectively) with five measurements, each comprising 10 runs.

TEM

Diluted samples of A647-CPMV-PEG5000 nanoparticles and A647-PVX-PEG5000 nanofilaments ($20~\mu L$., $0.1~mgmL^{-1}$) were negatively stained with of 2% (w/v) uranyl acetate for 2 min on a copper grid. Samples were analyzed using a Zeiss Libra 200FE transmission electron microscope operated at 200 kV.

Avian embryo tumor xenograft model

Fertilized chicken eggs (McKinley Hatchery, St. Mary's Ontario) were incubated in a rotary incubator (Berry Hill) under 70% humidity at 37°C for four days and then were removed from their shell and placed in sterile covered dishes. Avian embryos were incubated 5 more days in stationary incubators (Berry Hill) with 70% humidity at 37°C. On day 9, approximately 1×10⁵ HT1080GFP or HEp3GFP cells (which were cultured in DMEM medium with high glucose and L-glutamine, and supplemented with 10% FBS and 1% penicillin-streptomycin, all from Life Technologies) were injected in between the CAM layers and incubated for a further 6 days in stationary incubators with 70% humidity at 37°C to allow for tumor growth and vascularization. Embryos were then injected with a 100 µl mixture containing 120 µg of A555-PVX-PEG (490 A555/PVX) and 20 µg of A647-CPMV-PEG (60 A647/CPMV) in PBS (pH 7.4) to ensure delivery of equal number of particles. The embryos were imaged in each channel of interest before injection, right after injection, and each hour thereafter. Time-lapse images were captured with an epifluorescence wide-field microscope (Quorum; Zeiss Axio Examiner, Zeiss) and Volocity software v6.0.1 (Perkin Elmer) and further analyzed with Volocity. After 4 hours, the tumors were excised from the CAM, washed with PBS, and put into 10% sucrose and 3.7% formalin in PBS overnight at 4°C to fix the tissues and preserve fluorescence. Tumors were then washed in PBS and embedded with OCT on dry ice. Eight micron frozen sections of the tumor were collected (Leica CM1850 cryostat), mounted in Prolong gold with DAPI (Life Technologies), and imaged using an epifluorescence wide-field microscope attached to a spinning disc confocal unit (Quorum; Yokogawa CSU 10, Yokogawa) with Volocity software. Quantitation of nanoparticle uptake in HT1080GFP and HEp3GFP tumor xenograft models was determined by additional analysis of the acquired images in Volocity. Mean fluorescence within the tumor and core were quantified and further analyzed in GraphPad Prism v5.

Pharmacokinetics

Pharmacokinetics were evaluated using 8-week old healthy Balb/c animals (Charles River, MA). Following administration of A647-CPMV-PEG5000 and A647-PVX-PEG5000 formulations (200 $\mu g/100~\mu L)$ via tail vein injections, blood was collected over a period of 60 min through retro-orbital bleeding in mice using heparin-coated tubes (Fisher); 2 time points were taken per mouse. Plasma was recovered from the blood via centrifugation at 16,000 g for 10 min. Fluorescence intensity (Ex/Em wavelengths 600/665) was measured using a Tecan microplate reader.

Tumor homing of CPMV versus PVX using the NCR nu/nu mice with HT-29 xenografts

HT-29 cells (ATCC) were cultured in RPMI medium supplemented with 10% FBS, 1% penicillin-streptomycin, and 1% L-glutamine at 37°C in 5% CO₂ (tissue culture reagents

were supplied from Life Technologies). Tumors were induced through subcutaneous injection of 5×10⁶ cells/50 μL RPMI mixed with an equal volume of Matrigel (Fisher). Sixweek old NCR nu/nu mice were xenografted with HT-29 tumors on each flank. To reduce tissue autofluorescence, animals were maintained on an alfalfa free diet (Teklad) for two weeks prior to VNP administration. Animals were monitored and tumor size measured using calipers. Tumors were allowed to reach an average volume of 20 mm³ (10–12 days). A647-CPMV-PEG5000 (52 A647/CPMV) and A647-PVX-PEG5000 (385 A647/PVX) were administered intravenously at 200 μ g in 100 μ L of sterile PBS per mouse (n = 3 animals per group; groups: PBS, CPMV, and PVX). To ensure maximum tissue accumulation, we analyzed animals at t = 24 hrs post administration. Two methods were used to analyze tissue distribution based on fluorescence: (1) animals were sacrificed and brain, heart, lungs, spleen, kidneys, liver, as well as the tumors on the flanks were excised and imaged using MaestroTM fluorescence imaging instrument (using yellow excitation and emission filters with a 800 ms exposure time), and (2) tissues were collected, the weight recorded, and tissues were homogenized in PBS. Homogenates were centrifuged for 10 min at 13,000 g to remove non-homogenized tissue. Fluorescence intensity (Ex/Em wavelengths 600/665) was measured using a Tecan microplate reader. Data were normalized against tissue weight.

Immunohistochemistry

Intra-tumoral localization of CPMV and PVX was carried out using immunohistochemistry. Ten-micron thick tumor sections were prepared on a Leica CM1850 cryostat and fixed with 95% ethanol for 20 min in ice. Sections were then permeabilized with 0.2% Triton X-100 (EMD Chemicals) in PBS for 2 mins and rinsed with PBS. Blocking was done with 10% goat serum (GS) (Life Technologies) in PBS. Endothelium was immunostained using a FITC-labeled CD31 antibody (Biolegend) (1:250) with 1% GS for 1 h at room temperature (RT). The sectioned were rinsed thrice with PBS and nuclei were stained with DAPI (MP Biomedicals) (1:9500 in PBS) for 10 min at RT, followed with another round of rinsing with PBS. The sections were covered with Permount mounting media (Fisher). The slides were stored at -20°C until imaged. Confocal analysis of the stained tissue sections was carried out on Olympus FV1000 laser scanning confocal microscope.

RESULTS AND DISCUSSION

Production of CPMV and PVX

CPMV particles and PVX filaments were purified from infected *Vigna unguiculata* and *Nicotiana benthamiana* plants, respectively, yielding 0.5–1 mg VNPs per 1 g infected leaves. Virus concentration in plant extracts was determined by UV/visible spectroscopy (CPMV $\epsilon_{260~nm}=8.1~mLmg^{-1}cm^{-1}$ and PVX $\epsilon_{260~nm}=2.97~mLmg^{-1}cm^{-1}$). The purity of the VNP preparation was confirmed based on the A260:A280 ratio (a ratio of 1.8 indicates pure and intact CPMV particles, and a ratio of 1.2 indicates pure and intact PVX filaments). Structural integrity of the purified VNPs was further confirmed using transmission electron microscopy (TEM) as well as size-exclusion chromatography (SEC) (not shown).

Chemical modification of CPMV and PVX with polyethylene glycol (PEG) and Alexa Fluor 647 (A647)

VNPs are particulate and proteinaceous structures with high degree of symmetry and polyvalency. VNPs are thus intrinsically immunogenic materials. The immunogenicity of VNPs and many other proteinacous therapies can be significantly reduced through PEGylation ^{34–36}. The PEGylation of VNPs also reduces undesirable non-specific cell interactions, prolongs plasma circulation and increases stability^{28, 37, 38, 30, 39, 34}. PEG is thus an essential component when developing VNPs as contrast agents or drug delivery vehicles. We also incorporated Alexa Fluor 647 (A647); this near-infrared dye is commonly

used for molecular imaging applications and shows compatibility with the VNP carrier system as well as with fluorescent imaging modalities used in preclinical imaging, i.e. intravital microscopy and MaestroTM imaging system.

In this study, CPMV and PVX were labeled with PEG5000 and A647 (and A555) at solventexposed surface Lys residues using NHS active probes (Figure 1A). Purified A647-CPMV-PEG and A647-PVX-PEG were characterized using a combination of UV/visible spectroscopy, TEM, denaturing gel electrophoresis, and zeta potential measurements (Figure 1). TEM confirmed that VNPs remained structurally sound after chemical modification (Figure 1B). UV/visible measurements and electrophoresis of protein subunits confirmed that both labels, A647 (and A555, not shown) and PEG5000, were covalently attached. The number of dye moieties per VNP was calculated based on the UV/visible spectrum (not shown) using the concentration ratio of dye to VNP. The concentrations were calculated using Beer-Lambert law and the respective extinction coefficients: A647 $\epsilon_{650~nm}$ =270,000 $M^{-1}cm^{-1}$, CPMV $\epsilon_{260 \text{ nm}}$ =8.1 mLmg⁻¹cm⁻¹, and PVX $\epsilon_{260 \text{ nm}}$ =2.97 mLmg⁻¹cm⁻¹. Denaturing gel electrophoresis confirmed covalent modification of the coat proteins with A647 (this is based on the bright blue coloration of the protein bands when visualized under white light, not shown). Higher mobility bands indicate successful PEGylation (Figure 1C). Protein band intensity profile analysis using ImageJ software and Coomassie-stained gels was used to determine the degree of PEGylation.

We found that CPMV was labeled with 53 A647 dyes and 35 PEG5000 chains. PVX was found to display 386 A647 dyes and 380 PEG5000 chains. We found the reproducibility of generating these formulations lies within a 10% error range with regard to the number of fluorophores and PEG chains attached. CPMV consists of 60 copies each of a small and a large protein arranged in a pseudo *T*=3 symmetry; and PVX is formed by 1270 identical copies of a single coat protein arranged in helical structure. Data indicate similar degree of PEGylation comparing CPMV and PVX; in each case approximately 30 % of the coat proteins were labeled with PEG5000 chains (see also band intensity profile, Figure 1C). Considering the differences in molar mass of CPMV and PVX, the dye per protein ratio is comparable; 7.3x the number of dyes were attached to the 6.3x higher molecular weight macromolecule formed by PVX compared to CPMV (CPMV has a molar mass of 5.6×10⁶ gmol⁻¹, PVX has a molar mass of 35×10⁶ gmol⁻¹).

Overall engineered CPMV and PVX displayed similar degrees of surface modification with dyes and PEG. Of course, one has to take under consideration that each VNP is built from different coat protein building blocks and that ligand presentation differs based on the different geometrical shapes of the VNPs. Surface charge, in addition to carrier geometry, is an important factor to consider when comparing different materials. Therefore we determined the zeta potential of A647-CPMV-PEG and A647-PVX-PEG (Figure 1D). Fluorescent and PEGylated CPMV has a negative zeta potential of -16.4 ± 2.6 mV, whereas PVX has a positive zeta potential of 24.9 ± 8.2 mV. This is interesting considering that the reported isoelectric point of both VNPs are similar: the isoelectric point of CPMV lies between pH 3.4–4.5 and the isoelectric point of PVX is reported at pH 4.4 (dpvweb.net). When comparing these two VNPs differences in shape and zeta potential have to be taken into account (see discussion below).

It is important to note that in previous studies using PVX conjugated with A647 and PEG, an unexpected phenomenon was observed. When PVX was conjugated to A647 and PEG1000 cell interactions were reduced, as expected. However, when PVX was conjugated with A647 and PEG2000, increased cell interactions were reported ⁴⁰. This was demonstrated using HeLa and BalbCl7 cells. We hypothesized that the PEG2000 layer somehow stabilizes the A647 dye presentation on the VNP leading to enhanced interactions

of the hydrophobic flat molecule with the cell membrane. In the here-described studies, we revised the PVX design and incorporated PEG5000 (rather than PEG2000). We hypothesized that the larger PEG chains would efficiently cover the PVX rod including the A647 dyes and thus efficiently shield the nanomaterial from cellular interactions. Indeed, we confirmed using several mammalian cell lines that PVX-A647-PEG5000 is effectively shielded (see Supporting Information). The previously described phenomena are attributed to the specific combination of PVX, A647, and PEG2000. Since shielding and reduced cell interactions of A647-PVX-PEG5000 were confirmed, it is unlikely the *in vivo* properties of A647-PVX-PEG5000 are directed by the A647 fluorophore. The observations described below can be attributed to the physical and chemical differences between CPMV and PVX carriers.

Tumor homing and penetration of PVX *versus* CPMV in the avian embryo tumor xenograft model

Tumor homing and tissue penetration properties of CPMV and PVX VNPs were evaluated using human fibrosarcoma (HT1080) and squamous carcinoma (HEp3) tumor models. To evaluate tumor uptake in real time, intravital microscopy was carried out over a 4 hrs time frame (Figure 2A). The two VNPs were labeled with spectrally distinct fluorophores; A647-CPMV-PEG and A555-PVX-PEG were synthesized. This allowed for a direct side-by-side comparison of the two VNP platforms after co-injection. The amount of VNP administered was adjusted to give equal number of moles of VNP/animal, i.e. 120 μg of PVX and 20 μg CPMV were administered (3.5×10 $^{-12}$ moles VNP/animal). Intravital imaging indicated that both PVX and CPMV accumulated in solid tumors after intravenous administration; however, the intra-tumoral localization was found to differ with PVX accumulating in the center of the tumor (Figure 2B). A comparable tumor distribution was observed for both fibrosarcoma and squamous carcinoma tumor models.

Systemic delivery of nanocarriers and their cargos to solid tumors is largely governed through the enhanced permeability and retention (EPR) effect ⁴¹. EPR is characterized by increased vascular permeability and inefficient lymphatic drainage as a result of tumor hypervascularization. Nanomaterials passively target the tumor by extravasating from the tumor vasculature and accumulating in the tumor parenchyma. It has been shown previously that EPR-mediated accumulation of elongated nanomaterials is enhanced compared to spherical nanomaterials ^{2, 5}. In the CAM model, however, we did not observe enhanced tumor accumulation of the PVX *versus* CPMV. However, we did observe that PVX filaments homed to the tumor core, whereas CPMV nanoparticles were localized throughout the tissue with no apparent increase in the tumor center (Figure 2B). To further evaluate the intra-tumoral localization of PVX *versus* CPMV, tumors were collected, sectioned, and imaged using confocal microscopy. Consistent with findings from intravital imaging, PVX spread consistently throughout the tumor tissue and penetrated into areas in which CPMV was not apparent (Figure 2C).

A growing body of data indicates that filamentous structures have better diffusion rates in fibrous matrices (e.g. collagen-rich tumor matrices) compared to globular materials ^{42–46}, this may explain our observation that PVX penetrates deeper into the tumor tissue and accumulates in the tumor core. Besides the shape-derived advantages of PVX, surface charge-derived differences should also be considered. Consistent with our findings, others have reported enhanced tumor accumulation and penetration of positively charged materials. The collagen-rich matrix is a major determinant of interstitial transport ⁴⁷. Collagen carries positive charges and negatively-charged materials can aggregate in the collagen matrix through electrostatic interactions, thus limiting their diffusion rates. Cationic nanoparticles have enhanced tumor homing properties and also exhibit higher vascular permeability compared to their anionic counterparts ⁴⁴, ⁴⁵, ^{48–50}.

The positive zeta potential of PVX thus could further provide an advantage in addition to its flexible, high aspect ratio shape. Future experiments are required to separate charge and shape; this could be achieved through the display of negatively charged surface groups on PVX to invert its zeta potential. Alternatively, icosahedrons of the same size but opposite zeta potential could be evaluated, e.g. CPMV and *Brome mosaic virus* (BMV).

Tumor homing of CPMV versus PVX using the NCR nu/nu mice with HT-29 xenografts

Next, tumor homing and biodistribution of VNPs were evaluated using an animal model of colon cancer, specifically NCR nu/nu mice with human HT-29 xenografts. Tumors were allowed to reach an average volume of 20 mm³ (10–12 days) prior to administration of the VNPs. Quantitative studies were conducted using a combination of Maestro TM Imaging system and plate reader assays. The amount of protein and dyes were kept constant, i.e. 200 µg of A647-CPMV-PEG and A647-PVX-PEG, respectively were administered intravenously. Co-injection could not be performed. Even when animals were kept on an alfalfa-free diet the background fluorescence from tissues was too high for using dyes such as A488 or A555. Therefore both VNPs were labeled with A647 and evaluated side-by-side.

We found that, using the HT-29 tumor mouse model, PVX showed enhanced tumor homing compared to CPMV. Furthermore, the two VNPs show distinct biodistribution profiles (Figures 3–5). Results from imaging (Figure 3) and quantitative biodistribution (Figure 5) are in good agreement and it appears that CPMV nanoparticles are mostly localized to the liver with negligible tumor accumulation. In stark contrast, PVX showed enhanced tumor homing; PVX nanofilaments were also taken up by the liver and spleen.

Studying the intra-tumoral localization of A647-CPMV-PEG and A647-PVX-PEG on sectioned tumor tissues, it was found that neither formulation was confined within the endothelium. PVX accumulation is more profound, and it appears that PVX shows enhanced tissue penetration compared to CPMV; these findings are consistent with data from the avian tumor model (see Figure 2).

The enhanced tumor homing of PVX to solid tumors is consistent with reports on synthetic nanomaterials ^{2, 5}. Successful tumor delivery requires nanoparticles to enter tumor microcirculation followed by extravasation into tumor tissue. The fate of the nanoparticle depends on its ability to drift laterally toward the tumor blood vessel in order to extravasate into the surrounding tumor tissue. Filamentous rods have favorable margination properties compared to their spherical counterparts ^{6, 7, 51}. It also has been suggested that nanofilaments penetrate tumors better compared to spherical nanomaterials, thus further enhancing tumor retention, due to differences of nanoparticle *versus* nanofilament transport across membranes.

Enhanced plasma circulation times also can enhance tumor homing via EPR effects. Nanofilaments and rod-shaped materials tend to evade phagocytosis and thus have enhanced circulation times 52 . Interestingly, our data indicates that PEGylated and fluorescently-labeled CPMV, with a plasma half life of $t_{1/2}=20.8\,$ min, has a slightly longer plasma circulation time than PVX, which has a $t_{1/2}=12.5\,$ min (Figure 4). High accumulation of PVX was also observed in the spleen (Figures 3 and 5). Previous studies have indicated that positively-charged materials show prolonged plasma circulation times 53 . Therefore, it is somewhat surprising that filamentous PVX, with its high aspect ratio and high positive charge density does not show enhanced pharmacokinetics. Clearly, our data indicate that the enhanced tumor accumulation of PVX is governed by an alternate mechanism than enhanced plasma circulation time, and that the high uptake of PVX in the spleen may indicate rapid clearance through macrophages.

Biodistribution of CPMV and PVX are distinct

To gain further insight into the *in vivo* behavior of these VNPs, biodistribution was evaluated using fluorescently-labeled and PEGylated VNPs. At 24 hours post-intravenous administration, tissues were collected, digested, and the fluorescence intensity normalized to organ weight determined (Figure 5). CPMV accumulates predominantly in the liver (71% of administered CPMV is detected in the liver), while smaller amounts are detected in the spleen (13%) and 9% of the particles are localized to the tumor. PVX also accumulated in the liver (55%), however a significant amount is also found in the spleen (23%) and tumor homing is also enhanced with 15% of the administered dose (Figure 5).

Biodistribution of CPMV has been reported previously. CPMV has broad biodistribution and using PCR-based methods it could be detected in a wide variety of tissues throughout the body with no apparent toxic effects ^{13, 54}. Quantitative data indicated that CPMV particles mostly accumulated in the liver with some accumulation in the spleen ¹³. This is in good agreement with our findings (Figures 3 and 5). PVX also accumulates in the liver but also shows significant localization in the spleen. Uptake and accumulation of VNPs in organs with filtration function such as liver and spleen is expected. These organs are part of the reticuloendothelial system (RES), which is a component of the immune system. Its function is to remove antigens, such as proteinaceous nanoparticle structures, from circulation ⁵⁵. The fact that enhanced tumor homing was not observed in the CAM model could be explained by the differences in uptake by the RES, which is less developed in this embryonic model. Differences in the tumor homing profiles of CPMV and PVX were also observed in the CAM model. The high uptake of PVX in the spleen and its short plasma circulation time may indicate rapid clearance through macrophage uptake. In ongoing studies, it will be important to further evaluate the *in vivo* properties of PVX, specifically focusing on its immunogenicity and interactions with macrophages and other components of the immune system.

CONCLUSION

We report here that the filamentous, high aspect ratio PVX VNP platform shows enhanced tumor homing and tissue penetration properties compared to CPMV, the prototypical plant VNP. Our data suggest that there are shape- and surface charge-derived advantages of PVX for in vivo applications. This work lays the groundwork for the further development of PVX for applications in tissue-specific imaging and drug delivery. A full biodistribution, pharmacokinetics, and clearance study on PVX is forthcoming, but the high accumulation of PVX in the spleen suggests rapid clearance through macrophage uptake and could be related to the immunogenicity of the platform. Because PEGylation of the VNPs is expected to reduce macrophage uptake and interaction with cells of the immune system, it will be useful to evaluate the histopathology and immunogenicity of PVX in detail. Indeed, as the design principles are explored to engineer PVX as a drug delivery system, it will be important to achieve the correct balance between systemic clearance, tumor homing and tissue penetration. Certainly, this is one of the major challenges still facing cancer nanotechnology ⁴⁶. Filamentous VNP formulations have advantages beyond their physical and tumor homing properties. Rods have a much larger surface area than spherical particles, thus offering more potential acceptor sites for functionalization, and therefore greater loading with targeting ligands, imaging reagents and/or drugs. Rod-shaped particles also present ligands in a more efficient manner. Cells are typically 10-100 times larger than a nanostructure, and the cell surface tends to be relatively flat. A rod-shaped structure may in theory interact with a larger number of binding sites on the cell surface, thus potentially increasing targeting sensitivity and specificity. PVX is a promising new plant VNP technology, and the work presented here is in good agreement with the emerging paradigm that rod-shaped nanomaterials are advantageous for nanomedical applications.

Supplementary Material

Refer to Web version on PubMed Central for supplementary material.

Acknowledgments

This work was supported by NIH/NIBIB grants R00 EB009105 (to NFS), P30 EB011317 (to NFS), Mt. Sinai Foundation (to NFS), Prostate Cancer Canada grant 2011-742 (to JDL) and a NIH/NIBIB training grant T32 EB007509 (to AMW).

References

- 1. Cai S, Vijayan K, Cheng D, Lima EM, Discher DE. Micelles of Different Morphologies—Advantages of Worm-like Filomicelles of PEO-PCL in Paclitaxel Delivery. Pharm Res. 2007; 24:2099–2109. [PubMed: 17564817]
- Chauhan VP, et al. Fluorescent nanorods and nanospheres for real-time in vivo probing of nanoparticle shape-dependent tumor penetration. Angew Chem Int Ed. 2011; 50:11417–11420.
- 3. Christian DA, et al. Flexible filaments for in vivo imaging and delivery: persistent circulation of filomicelles opens the dosage window for sustained tumor shrinkage. Mol Pharm. 2009; 6:1343–1352. [PubMed: 19249859]
- 4. Decuzzi P, et al. Size and shape effects in the biodistribution of intravascularly injected particles. Journal of Controlled Release. 2010; 141:320–327. [PubMed: 19874859]
- Geng Y, et al. Shape effects of filaments versus spherical particles in flow and drug delivery. Nat Nanotechnol. 2007; 2:249–255. [PubMed: 18654271]
- 6. Gentile F, et al. The effect of shape on the margination dynamics of non-neutrally buoyant particles in two-dimensional shear flows. J Biomech. 2008; 41:2312–2318. [PubMed: 18571181]
- Lee SY, Ferrari M, Decuzzi P. Shaping nano-/micro-particles for enhanced vascular interaction in laminar flows. Nanotechnology. 2009; 20:49510.
- 8. Firme CP 3rd, Bandaru PR. Toxicity issues in the application of carbon nanotubes to biological systems. Nanomedicine. 2010; 6:245–256. [PubMed: 19699321]
- 9. Chitale R. Merck hopes to extend gardasil vaccine to men. J Natl Cancer Inst. 2009; 101:222–223. [PubMed: 19211446]
- Liu TC, Galanis E, Kirn D. Clinical trial results with oncolytic virotherapy: a century of promise, a decade of progress. Nat Clin Pract Oncol. 2007; 4:101–117. [PubMed: 17259931]
- 11. Shirakawa T. Clinical trial design for adenoviral gene therapy products. Drug News Perspect. 2009; 22:140–145. [PubMed: 19440556]
- Kaiser CR, et al. Biodistribution studies of protein cage nanoparticles demonstrate broad tissue distribution and rapid clearance in vivo. Int J Nanomedicine. 2007; 2:715–733. [PubMed: 18203438]
- 13. Singh P, et al. Bio-distribution, toxicity and pathology of cowpea mosaic virus nanoparticles in vivo. J Control Release. 2007; 120:41–50. [PubMed: 17512998]
- 14. Pokorski JK, Steinmetz NF. The art of engineering viral nanoparticles. Mol Pharm. 2011; 8:29–43. [PubMed: 21047140]
- 15. Anderson EA, et al. Viral nanoparticles donning a paramagnetic coat: conjugation of MRI contrast agents to the MS2 capsid. Nano Lett. 2006; 6:1160–1164. [PubMed: 16771573]
- Hooker JM, Datta A, Botta M, Raymond KN, Francis MB. Magnetic resonance contrast agents from viral capsid shells: a comparison of exterior and interior cargo strategies. Nano Lett. 2007; 7:2207–2210. [PubMed: 17630809]
- 17. Hooker JM, O'Neil JP, Romanini DW, Taylor SE, Francis MB. Genome-free viral capsids as carriers for positron emission tomography radiolabels. Mol Imaging Biol. 2008; 10:182–191. [PubMed: 18437498]
- Kovacs EW, et al. Dual-surface-modified bacteriophage MS2 as an ideal scaffold for a viral capsid-based drug delivery system. Bioconjug Chem. 2007; 18:1140–1147. [PubMed: 17602681]

19. Loo L, Guenther RH, Lommel SA, Franzen S. Encapsidation of nanoparticles by red clover necrotic mosaic virus. J Am Chem Soc. 2007; 129:11111–11117. [PubMed: 17705477]

- Loo L, Guenther RH, Lommel SA, Franzen S. Infusion of dye molecules into Red clover necrotic mosaic virus. Chem Commun. 2008:88–90.
- 21. Ren Y, Wong SM, Lim LY. In vitro-reassembled plant virus-like particles for loading of polyacids. J Gen Virol. 2006; 87:2749–2754. [PubMed: 16894216]
- 22. Ren Y, Wong SM, Lim LY. Folic acid-conjugated protein cages of a plant virus: a novel delivery platform for doxorubicin. Bioconjugate Chem. 2007; 18:836–843.
- 23. Suci PA, et al. High-density targeting of a viral multifunctional nanoplatform to a pathogenic, biofilm-forming bacterium. Chem Biol. 2007; 14:387–398. [PubMed: 17462574]
- Suci PA, Varpness Z, Gillitzer E, Douglas T, Young M. Targeting and photodynamic killing of a microbial pathogen using protein cage architectures functionalized with a photosensitizer. Langmuir. 2007; 23:12280–12286. [PubMed: 17949022]
- Bruckman MA, et al. Surface modification of tobacco mosaic virus with "click" chemistry. Chembiochem. 2008; 9:519–523. [PubMed: 18213566]
- Rong J, et al. Oriented cell growth on self-assembled bacteriophage M13 thin films. Chem Commun. 2008:5185–5187.
- 27. Souza GR, et al. Three-dimensional tissue culture based on magnetic cell levitation. Nat Nanotechnology. 2010; 5:291–296.
- 28. Lewis JD, et al. Viral nanoparticles as tools for intravital vascular imaging. Nat Medicine. 2006; 12:354–360.
- 29. Steinmetz NF, et al. Intravital imaging of human prostate cancer using viral nanoparticles targeted to gastrin-releasing Peptide receptors. Small. 2011; 7:1664–1672. [PubMed: 21520408]
- 30. Steinmetz NF, Cho CF, Ablack A, Lewis JD, Manchester M. Cowpea mosaic virus nanoparticles target surface vimentin on cancer cells. Nanomedicine. 2011; 6:351–364. [PubMed: 21385137]
- 31. Chatterji A, et al. New addresses on an addressable virus nanoblock: uniquely reactive Lys residues on cowpea mosaic virus. Chem Biol. 2004; 11:855–863. [PubMed: 15217618]
- 32. Steinmetz NF, et al. Potato virus X as a novel platform for potential biomedical applications. Nano letters. 2010; 10:305–312. [PubMed: 20017489]
- 33. Wellink J. Comovirus isolation and RNA extraction. Methods Mol Biol. 1998; 81:205–209. [PubMed: 9760508]
- 34. Raja KS, et al. Hybrid virus-polymer materials. 1. Synthesis and properties of PEG-decorated cowpea mosaic virus. Biomacromolecules. 2003; 4:472–476. [PubMed: 12741758]
- 35. Le HT, Yu QC, Wilson JM, Croyle MA. Utility of PEGylated recombinant adeno-associated viruses for gene transfer. J Control Release. 2005; 108:161–177. [PubMed: 16125817]
- 36. Lee GK, Maheshri N, Kaspar B, Schaffer DV. PEG conjugation moderately protects adeno-associated viral vectors against antibody neutralization. Biotechnol Bioengg. 2005; 92:24–34.
- 37. Destito G, Yeh R, Rae CS, Finn MG, Manchester M. Folic acid-mediated targeting of cowpea mosaic virus particles to tumor cells. Chem Biol. 2007; 14:1152–1162. [PubMed: 17961827]
- 38. Brunel FM, et al. Hydrazone ligation strategy to assemble multifunctional viral nanoparticles for cell imaging and tumor targeting. Nano Lett. 2010; 10:1093–1097. [PubMed: 20163184]
- Steinmetz NF, Manchester M. PEGylated viral nanoparticles for biomedicine: the impact of PEG chain length on VNP cell interactions in vitro and ex vivo. Biomacromolecules. 2009; 10:784–792. [PubMed: 19281149]
- 40. Steinmetz NF, et al. Potato virus X as a novel platform for potential biomedical applications. Nano Lett. 2010; 10:305–312. [PubMed: 20017489]
- 41. Iyer AK, Khaled G, Fang J, Maeda H. Exploiting the enhanced permeability and retention effect for tumor targeting. Drug Discovery Today. 2006; 11:812–818. [PubMed: 16935749]
- 42. Nederman T, Acker H, Carlsson J. Penetration of substances into tumor tissue: a methodological study with microelectrodes and cellular spheroids. In Vitro. 1983; 19:479–488. [PubMed: 6347871]
- 43. Netti PA, Berk DA, Swartz MA, Grodzinsky AJ, Jain RK. Role of extracellular matrix assembly in interstitial transport in solid tumors. Cancer Res. 2000; 60:2497–2503. [PubMed: 10811131]

44. Stylianopoulos T, Diop-Frimpong B, Munn LL, Jain RK. Diffusion anisotropy in collagen gels and tumors: the effect of fiber network orientation. Biophys J. 2010; 99:3119–3128. [PubMed: 21081058]

- 45. Stylianopoulos T, et al. Diffusion of particles in the extracellular matrix: the effect of repulsive electrostatic interactions. Biophys J. 2010; 99:1342–1349. [PubMed: 20816045]
- 46. Thurber GM, Schmidt MM, Wittrup KD. Antibody tumor penetration: Transport opposed by systemic and antigen-mediated clearance. Adv Drug Deliv Rev. 2008; 60:1421–1434. [PubMed: 18541331]
- 47. Jain RK, Stylianopoulos T. Delivering nanomedicine to solid tumors. Nat Rev Clin Oncol. 2010; 7:653–664. [PubMed: 20838415]
- 48. Campbell RB, et al. Cationic charge determines the distribution of liposomes between the vascular and extravascular compartments of tumors. Cancer Res. 2002; 62:6831–6836. [PubMed: 12460895]
- Dellian M, Yuan F, Trubetskoy VS, Torchilin VP, Jain RK. Vascular permeability in a human tumour xenograft: molecular charge dependence. Br J Cancer. 2000; 82:1513–1518. [PubMed: 10789717]
- Schmitt-Sody M, et al. Neovascular targeting therapy: paclitaxel encapsulated in cationic liposomes improves antitumoral efficacy. Clin Cancer Res. 2003; 9:2335–2341. [PubMed: 12796403]
- 51. Toy R, Hayden E, Shoup C, Baskaran H, Karathanasis E. The effects of particle size, density and shape on margination of nanoparticles in microcirculation. Nanotechnology. 2011; 22:115101. [PubMed: 21387846]
- 52. Champion JA, Mitragotri S. Role of target geometry in phagocytosis. Proc Natl Acad Sci U S A. 2006; 103:4930–4934. [PubMed: 16549762]
- Li SD, Huang L. Pharmacokinetics and Biodistribution of Nanoparticles. Mol Pharm. 2008; 5:496–504. [PubMed: 18611037]
- 54. Rae CS, et al. Systemic trafficking of plant virus nanoparticles in mice via the oral route. Virology. 2005; 343:224–235. [PubMed: 16185741]
- 55. Peiser L, Mukhopadhyay S, Gordon S. Scavenger receptors in innate immunity. Curr Opin Immunol. 2002; 14:123–128. [PubMed: 11790542]

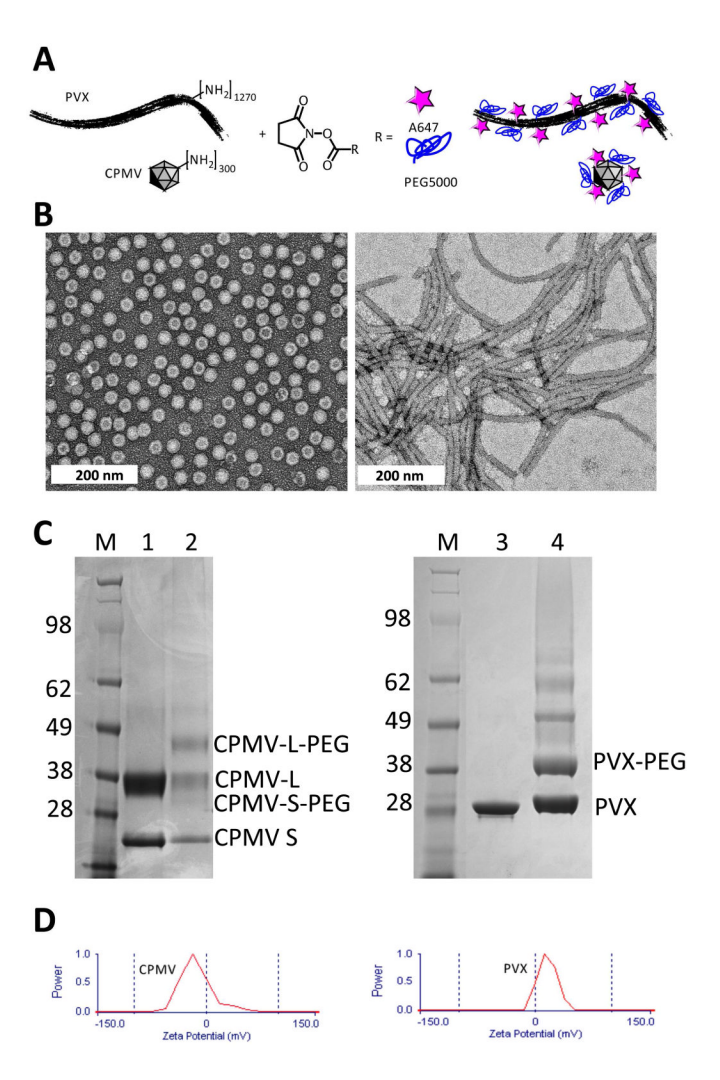


Figure 1. A) Bioconjugation scheme showing A647 and PEG5000 conjugation to solvent-exposed Lys side chains on PVX and CPMV. **B)** TEM of negatively-stained (2% w/v UAc) A647-CPMV-PEG (left) and A647-PVX-PEG5000 (right). **C)** SDS gel after Coomassie staining of separated coat proteins. M = SeeBlue Plus2 protein marker, numbers indicate molecular weight standards in kDa. 1 = CPMV, 2 = A647-CPMV-PEG, 3 = PVX, and 4 = A647-PVX-PEG5000. CPMV consists of S and L protein; PVX consists of a single coat protein. Lower mobility bands indicate PEGylation. Band density analysis was performed using band analysis tool and ImageJ software. **D)** Zeta potential of A647-labeled and PEGylated VNPs.

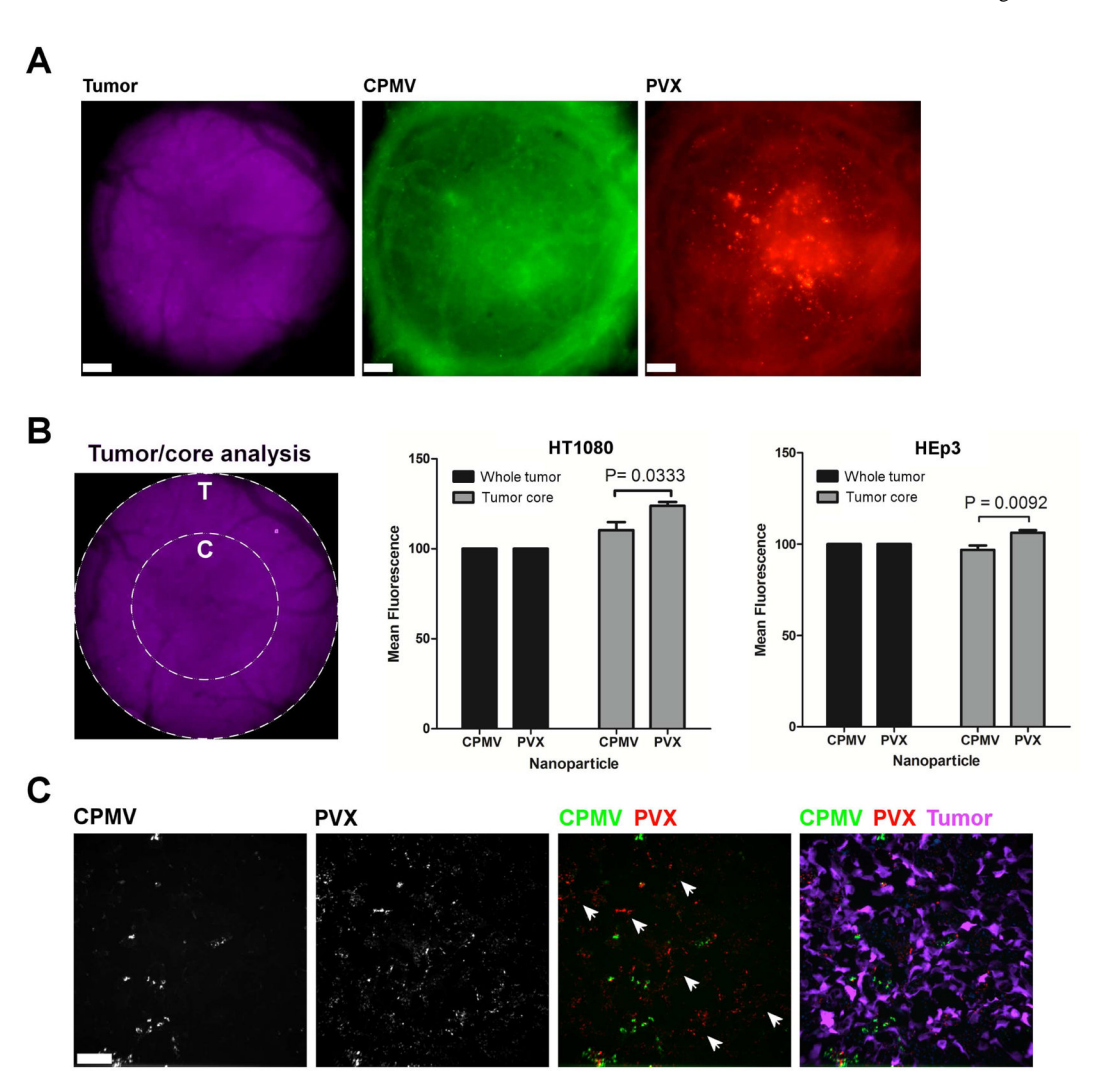


Figure 2. Intravital imaging of VNP uptake in human tumor xenografts in the CAM A. Avian embryos bearing vascularized GFP-expressing human fibrosarcoma HT1080 or human epithelial carcinoma HEp3 tumors (magenta) were co-injected with 120 μg of PVX-PEG-A555 (red) and 20 μg of CPMV-PEG-647 (green) and visualized 4 h after injection. Scale bar = 190 μm . B. The analysis of whole tumor uptake of CPMV and PVX nanoparticles compared to uptake only in the tumor core was assessed using distinct ROIs (left panel) in HT1080 (middle panel) and HEp3 (right panel) tumors. While whole tumor localization of CPMV and PVX were comparable, PVX accumulated in the core of tumors to a significantly higher degree than CPMV (unpaired t test). C. The localization of nanoparticles was assessed in 8 micron sections of the tumor core using fluorescence microscopy. CPMV (green) and PVX (red) are visualized in the tumor (magenta). While CPMV was visualized in punctate foci, PVX was distributed throughout the tumor in areas devoid of CPMV (white arrowheads).

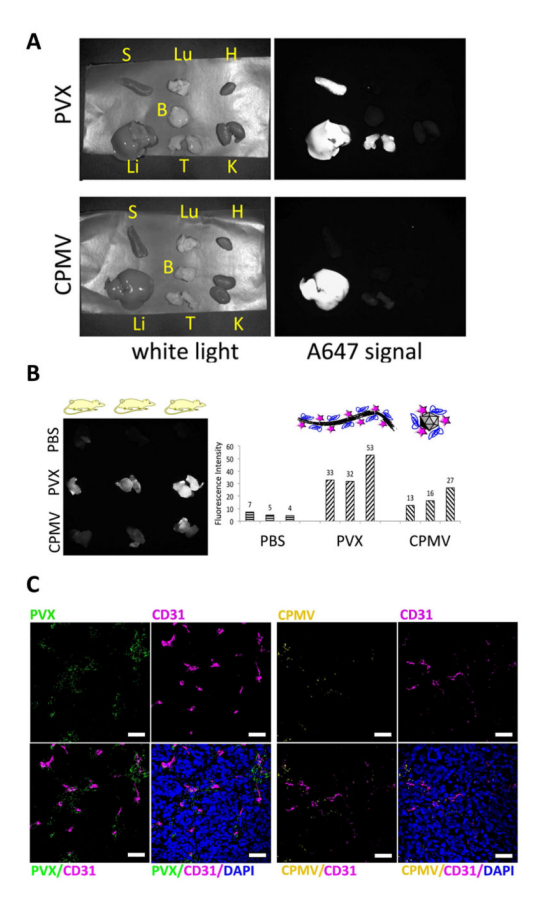
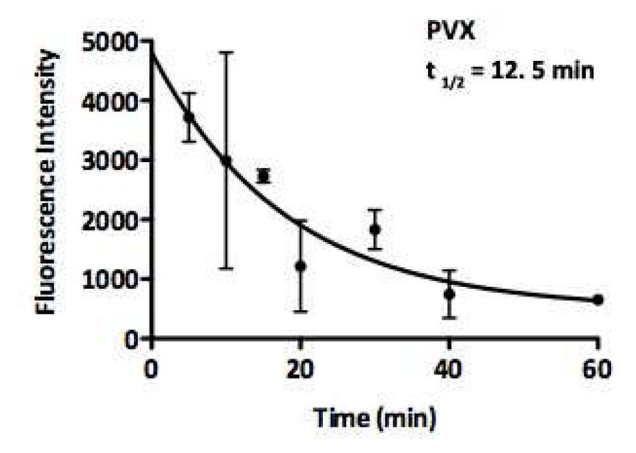


Figure 3. Tumor homing and biodistribution of VNPs measured using Maestro[™] Imager A) A647-labeled and PEGylated CPMV and PVX were administered intravenously into nude mice bearing HT-29 xenografts. 24-hours post-injection tissues were collected and imaged; tissues are shown under white light and fluorescence (A647 signal). B) Tumors (2 per animal) were exercised from 3 animals and imaged; qualitative data (left) and quantitative data (right) are presented. C) Intra-tumoral localization of CPMV (pseudocolored in yellow) and PVX (pseudo-colored in red). Endothelium was immunostained using a FITC-labeled CD31 antibody (pseudocolored in pink). Nuclei were stained with DAPI (blue). Scale bars are 30 microns.



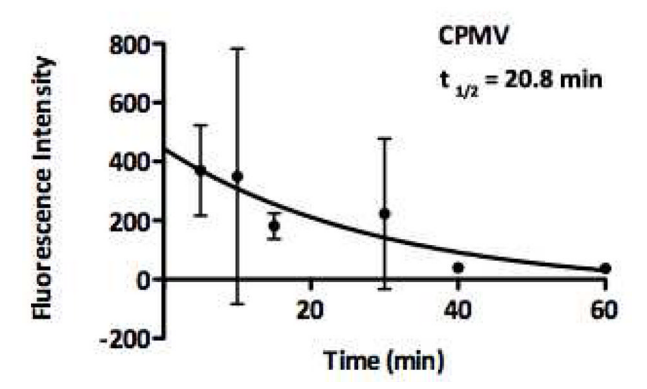
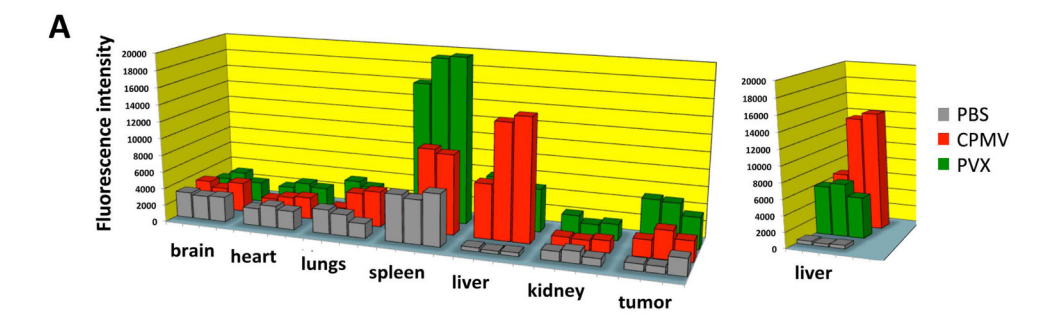


Figure 4. Plasma clearance of A647-labeled, PEGylated PVX and CPMVPharmacokinetics were evaluated using healthy Balb/c mice. Blood was collected over a 60-min time period, plasma extracted and the fluorescence intensity measured.



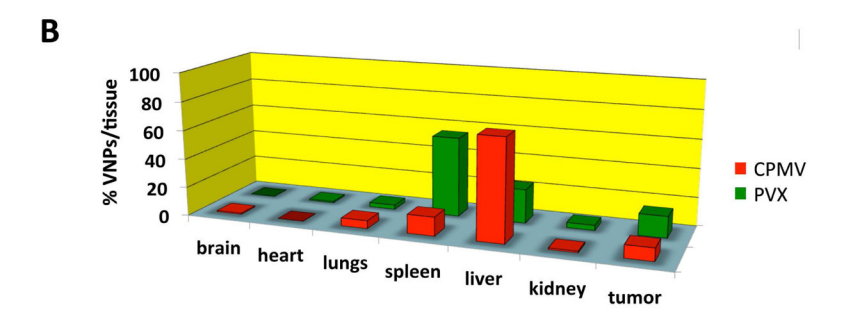


Figure 5. A) Biodistribution of A647-labeled and PEGylated CPMV and PVX nanoparticles and filaments. Three nude mice with human HT-29 tumor xenografts each were injected with PBS (control group), CPMV, and PVX. Tissues were collected and analyzed 24 h post administration. Fluorescence intensity normalized per gram of tissue weight is plotted for all major organs and tumors for each mouse. **B)** Average biodistribution normalized against PBS samples. The percentage of VNPs detected in each tissue is shown for each organ and tumors analyzed.